Kelvin-Helmholtz instability in the presence of variable viscosity for mudflow resuspension in estuaries

Alice Harang, Olivier Thual, Pierre Brancher, Thomas Bonometti

Université de Toulouse; INPT, UPS; IMFT, Allée Camille Soula, F-31400 Toulouse, France
CNRS; IMFT ; F-31400 Toulouse, France

Abstract

The temporal stability of a parallel shear flow of miscible fluid layers of different density and viscosity is investigated through a linear stability analysis and direct numerical simulations. The geometry and rheology of this Newtonian fluid mixing can be viewed as a simplified model of the behavior of mudflow at the bottom of estuaries for suspension studies. In this study, focus is on the stability and transition to turbulence of an initially laminar configuration. A parametric analysis is performed by varying the values of three control parameters, namely the viscosity ratio, the Richardson and Reynolds numbers, in the case of initially identical thickness of the velocity, density and viscosity profiles. The range of parameters has been chosen so as to mimic a wide variety of real configurations. This study shows that the Kelvin-Helmholtz instability is controlled by the local Reynolds and Richardson numbers of the inflection point. In addition, at moderate Reynolds number, viscosity stratification has a strong influence on the onset of instability, the latter being enhanced at high viscosity ratio, while at high Reynolds number, the influence is less pronounced. In all cases, we show that the thickness of the mixing layer (and thus resuspension) is increased by high viscosity stratification, in particular during the non-linear development of the instability and especially pairing processes. This study suggests that mud viscosity has to be taken into account for resuspension parameterizations because of its impact on the inflection point Reynolds number and the viscosity ratio, which are key parameters for shear instabilities.

Keywords: Transition to turbulence; Instability, Stratified flows; Mixing and dispersion; Geophysical Flows.
PACS: 47.20.-k; 47.11.-j; 47.85.-g; 47.51.+a.

1 Introduction

The motivation of this article is to complement experiments and observations on the lutocline (the interface between mudflow and water) at the bottom of estuaries, in order to get a better understanding of its dynamics and to improve the parameterizations of the entrainment mass and momentum fluxes. Numerical models of estuaries (Le Normant, 2000; Cugier and Le Hir, 2002; Le Hir et al, 2011) deal with pollution or coastal settlement. These models of sedimentary transport use parameterization of suspended matter fluxes at the bottom boundary condition. Cohesive materials (muds) present a more complex behavior than non-cohesive ones (sands) and are much less documented (see McAnally et al, 2007a). As explained by McAnally et al (2007b), the behavior of mud flows and their dynamical processes are still misunderstood since "the formulation of constitutive relations are dependent on empirical relationships based on small data sets". Concerning mud erosion, different models have been used, depending on the level of consolidation of the material (or sediment concentration), size distribution of sediment or erosion depth (Partheniades, 1965; Odd and Cooper, 1989; Srinivas and Mehta, 1989; Neumeier et al, 2008; Amos et al, 2010). Consolidated muds erosion principally relies on a critical bottom shear whereas fluid mud entrainment also depends on the Richardson number (Odd and Cooper, 1989; Srinivas and Mehta, 1989). The erosion fluxes computed in these models depend on the hydrodynamic fields at the mud-water interface such as the velocity shear or the density stratification. To improve the understanding of the underlying processes such as erosion, a study of the hydrodynamical processes governing this interface is necessary. As differents authors focused on turbulent equilibrium at the interface (Kranenburg and Winterwerp, 1997; Ozdemir et al, 2011), the transition to turbulence and the role of shear instability, observed on lutoclines (Adams et al, 1993) and in laboratory experiments (Mehta and Srinivas, 1993), are studied here for a better understanding of mud flow entrainment.

Shear instability studies of stratified shear flows are abundant in the literature. Helmholtz (1868) and Kelvin (1871) investigated the configuration of two layers with vanishing shear thickness. Rayleigh (1879) showed that the velocity profile needs to have an inflectional point to be possibly unstable in the unstratified case and generalized the stability analysis to non-zero stratification thickness. From the theoretical works of Orr (1907) and Sommerfeld (1908), the equation of perturbations in a parallel flow, known as the Orr-Sommerfeld equation were derived. Drazin and Reid (1984) proposed an overview of this commonly named "Kelvin-Helmholtz" or KH instability. It was shown that a density stratification stabilizes shear flows since those are stable when the local Richardson number is everywhere greater than 1/4 (Miles, 1961).

Confinement was first explored by Rayleigh (1879): he showed that symmetric boundary conditions have a stabilizing effect on inviscid KH instability. If the confinement is sufficiently strong, the flow becomes stable (Drazin and Reid, 1984). Healey (2009) presented the possible destabilizing effect of asymmetric confinement on absolute instability, although negligible for temporal stability.

The non-linear evolution of the KH instability into an array of corotating vor-

tices and the development of secondary instabilities has been addressed through both laboratory and numerical experiments. The two-dimensional evolution of the instability was presented in Corcos and Sherman (1984) and Patnaik et al (1976). KH rolls evolve with the development of sub-harmonics and pairing. Fontane and Joly (2008) focused on the stability for variable density KH rolls. They located the development of a secondary instability in the vorticity-enhanced braid by computing possible modes of this secondary instability. Three-dimensionnalisation of the flow was considered by Corcos and Lin (1984) and mixing efficiency of these instabilities was presented in Peltier and Caulfield (2003). Staquet (1995) explored 2D configuration finding a new kind of secondary instability, consisting in the development of a vortex at the inflectional point of the braid. 3D simulations to study secondary instabilities had been carried by Staquet (2000) and Mashayek and Peltier (2011). By using observations of an estuarian pycnocline, Geyer et al (2010) proposed a different behavior of primary billows. Mainly, experiments and simulations were carried out for low or intermediate Reynolds number whereas in the ocean or in the atmosphere, the Reynolds numbers are important (of the order of 10^6). The authors observed the conservation of the primary structure associated with the development of secondary shear instability on the braid, mainly responsible for the mixing.

When the thickness of the density profile is larger than the one of the shear, as often observed in stratified natural fields (Carpenter et al, 2010), the KH instability can coexist with two other main kinds of instabilities, namely the Taylor and Holmboe instabilities. Following the initial work of Taylor (1931) and Holmboe (1962), Caulfield (1994) defined their domain of development and the characteristics of their linear growth. Focus is now on their evolution and mixing properties (see Balmforth et al, 2012).

Alongside with stratified shear instability, instabilities of viscous layered flows were explored, initially by Yih (1967). For plane Poiseuille-Couette flows of different viscosities, he observed two different modes: the Tollmien-Schlichting instability well-known in homogen fluids and a "soft mode", also denoted by "Yih mode" or "interfacial mode". For all Reynolds numbers, the Yih mode is unstable for long wave disturbances, if the most viscous layer is also the thinnest. The mechanism of the viscous instability, studied by Hinch (1984) and Hooper and Boyd (1983), involves the continuity of shear stress at the interface. Malik and Hooper (2005) explored the behavior of miscible flow layer by opposition to two-fluid flows. He showed that, contrarily to the case of two-fluid flow, the miscible flow layer behaves like a homogeneous flow when the viscosity ratio vanishes. If miscible flow layers present an interface larger than $(k^*Re)^{1/3}$, there is no interfacial modes and the stability is determined by shear modes. Govindarajan (2004) also studied miscible flow layer and observed a third kind of instability, the overlap mode, in addition the shear and interfacial modes. Diffusion can be destabilizing, as seen in Ern et al (2003) for continuous but rapidly varying stratification profiles, or in Sahu et al (2009) for coaxial configurations. In a study of the two layer interface of fluids with different viscosities and rheologies, Ozgen et al (1998) explored the influence of density stratification on the Yih modes.

As KH instability is a non-viscous process, viscosity has little influence on the

development of the primary billows. However, when viscous diffusion can no longer be neglected as compared with inertia, the development of this instability is inhibited for intermediate Reynolds numbers. To our knowledge, the influence of viscous and density stratifications on the evolution of the instability and its final mixing is not documented in the literature. Some works like Govindarajan (2004) give informations on the influence of miscible interface of viscosity in coaxial configurations, but do not focus on its influence on KH modes.

In order to improve the understanding of the processes acting at the lutocline, such as entrainment, we present here a two-dimensional study of the hydrodynamical processes governing this interface, by modeling the mud flow by a dense and viscous Newtonian fluid. In the present work, we focus on profiles of same thickness for density, viscosity and velocity in order to examine, more particularly, the influence of viscosity stratification on Kelvin-Helmholtz instabilities and final thickness of the mixing layer. The model equations, the flow configuration and the numerical solvers are presented in Section 2. Results of the linear development of the instability are presented in Section 3. Section 4 presents the non-linear evolution of the instability through 2D direct numerical simulations, including a discussion on possible three-dimensional effects. Conclusions are given in the final section and a detailed description of the method used for the linear stability study is given in the appendix.

2 Equations and numerical approaches

2.1 Equations for the modeling of mud flows

Mud particles, whose diameter is under 60μm, present a Stokes number of the order of 10^{-4}. However, for rapid events such as resuspension, they can be considered inertial. Thus, in the present work, mud is modeled by a homogeneous fluid of higher density and viscosity than water, in the presence of gravity $\mathbf{g}$. With these assumptions, the flow is governed by the following equations:

$$\nabla \cdot \mathbf{u} = 0 \,, \qquad \frac{\partial \mathbf{u}}{\partial t} + (\mathbf{u} \cdot \nabla)\mathbf{u} = -\frac{1}{\rho}\nabla p + \mathbf{g} + \frac{1}{\rho}\nabla \cdot \left[\mu \left(\nabla \mathbf{u} + {}^{t}\nabla \mathbf{u}\right)\right], \quad (1)$$

$$\frac{\partial \phi}{\partial t} + \nabla \cdot (\phi \, \mathbf{u}) = 0, \qquad (2)$$

$$\rho = \phi \, \rho_1 + (1 - \phi) \, \rho_2, \qquad \mu = \phi \, \mu_1 + (1 - \phi) \, \mu_2, \qquad (3)$$

which links the incompressible Navier-Stokes equations (1) for the pressure p and the velocity field $\mathbf{u} = (u, v, w)$, to the transport equation of volume fraction ϕ of the mud flow in the fluid. Local properties of the fluid, such as density ρ and molecular dynamic viscosity μ, are calculated from this volume fraction ϕ. The two following fluids are considered: water, of density ρ_2 and dynamic viscosity μ_2, and mud flow, modeled by a Newtonian fluid of density $\rho_1 > \rho_2$ and viscosity $\mu_1 \geq \mu_2$. In this configuration, density and viscosity are linear functions of the volume fraction ϕ and, therefore, vary in the same manner. We have chosen the case of an infinite Schmidt

4

number: mud diffusion in water is neglected compared to momentum diffusion. This explains the absence of diffusion term in Equation (2) dealing with the transport of the volume fraction. This choice is consistent with the fact that mud particle diffusion is weaker than salt diffusion, which is itself less important than viscosity by a factor of $Pr \sim 700$, in laminar configurations, where Pr is the salt-stratified water Prandtl number. This choice is rather atypical for fine sediment modeling. If the flow were no longer considered laminar, mass diffusion could no longer be neglected.

2.2 Flow configuration

Lets us consider a domain of length L and height $H = 3$ m. Here x (resp. z) is the streamwise (resp. vertical) direction. This domain is filled at the bottom by a horizontal layer of mud, the characteristic thickness of which being $h = 1$ m. The initial flow configuration is depicted in figure 1.
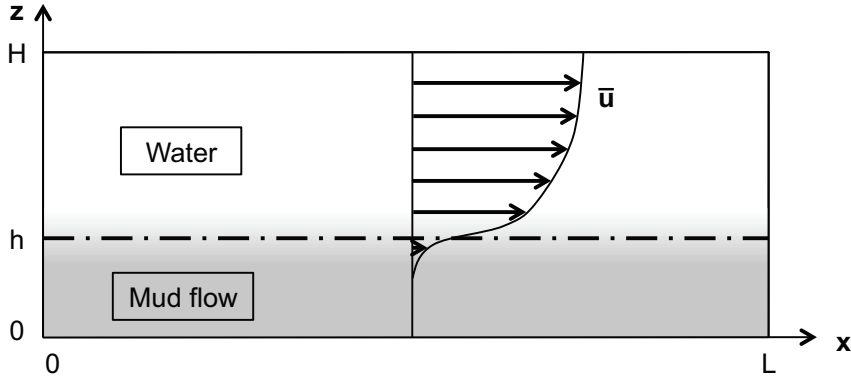

Figure 1: Initial flow configuration. Streamwise velocity $\bar{u}$, density $\bar{\rho}$ and viscosity $\bar{\mu}$ are function of z.

We consider a base flow of the form $\mathbf{u} = (\bar{u}(z), 0, 0)$ and $\phi = \bar{\phi}(z)$, in which the pressure is hydrostatic. We suppose that $\bar{u}(z)$ and $\bar{\phi}(z)$ are monotonous and differentiable functions with respective extreme values $\bar{u} = u_1$ and $\bar{\phi} = 1$ at the bottom of the domain, and $\bar{u} = u_2$ and $\bar{\phi} = 0$ at its top, with $u_1 < u_2$. We assume that the two profiles have a single inflection point at $z = h$. In other words, we neglect the effect of friction at the bottom and top boundary. This is reasonable since we are interested by shear-induced resuspension in the region close to the interface $z = h$. We then define the "inflection point thicknesses" associated with each velocity and volume fraction profiles by

$$\delta_u = \frac{u_2 - u_1}{2\,\bar{u}'(h)} \qquad \text{and} \qquad \delta_\phi = \frac{1}{2\,\bar{\phi}'(h)} \,, \tag{4}$$

where the prime denotes the z-derivation. In the present work, we assume δ_u and δ_ϕ to be equal to a same value denoted by δ. The most general case of $\delta_u \neq \delta_\phi$ is left for future work.
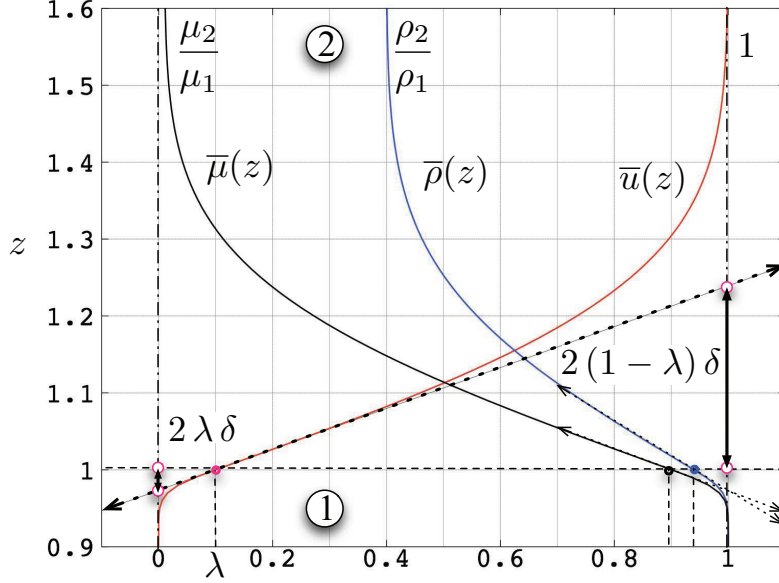
5

Figure 2: Initial profiles of $\overline{u}(z)$, $\overline{\rho}(z)$ and $\overline{\mu}(z)$ on a portion $z \in [0.9 \text{ m}, 1.6 \text{ m}]$ with $h = 1$ m, $4\delta/\sqrt{\pi} = 0.3$ m and $\lambda = 0.1$.

To model base flows representative of the density, viscosity and velocity fields observed at water-mud flow interface, we consider the group of functions $F(\lambda, Z)$ defined by:

$$F(\lambda, Z) = \begin{cases} \lambda \left[1 + \text{erf}\left(\frac{Z}{\lambda}\right)\right] & \text{if } Z \leq 0, \\ 1 - (1-\lambda)\left[1 - \text{erf}\left(\frac{Z}{1-\lambda}\right)\right] & \text{if } Z \geq 0, \end{cases} \tag{5}$$

where Z is a non-dimensional vertical coordinate, the origin of which is located at the interface. The dimensionless parameter λ controls the asymmetry between both sides of the inflection point (figure 2). Symmetrical profiles of the gradient correspond to $\lambda = 0.5$. For $\lambda < 0.5$ (resp. $\lambda > 0.5$), the lower part is thinner (resp. thicker) than the upper part. One can easily check the continuity of the profiles and its derivatives around this point. We then defined the base flow and volume fraction by

$$\bar{u}(z) = u_2 \, F\left(\lambda, \frac{z-h}{\delta} \frac{\sqrt{\pi}}{4}\right) \qquad \text{and} \qquad \bar{\phi}(z) = 1 - F\left(\lambda, \frac{z-h}{\delta} \frac{\sqrt{\pi}}{4}\right), \tag{6}$$

where $\delta = \delta_u = \delta_\phi$ is consistent with the definitions of Equation (4).

These profiles are considered here as quasi-steady states of (1)-(3) since we assume that the growth time of their instabilities is small compared to the diffusion time. Such an assumption will be verified a posteriori by comparing the growth of the equilibrium stability analysis to the one given by the direct numerical simulations. As shown later, both approaches lead to the same growth rate, giving further support that the present quasi-steady state hypothesis is justified.

6

The empirical erf(Z) functions qualitatively model a simple shear. As we consider profiles with high viscosity stratification at the interface, associated with shear velocity profiles, an important variation of the local Reynolds number is observed through the interface. In the upper layer, high Reynolds number implies turbulent flow associated with high turbulent diffusion. At the inflection point and in the lower layer, smaller Reynolds number induces laminar flow (in the context of estuarine parameters). This evolution of the Reynolds number motivates the choice of the present base flow profiles, which are adapted to high viscosity stratification. Moreover, they are also chosen because they closely mimic the ones observed in practical situations (see Mehta et al, 1989; Wolanski et al, 1989; Adams et al, 1993). Then, as laminar flow is supposed at the interface for high viscosity stratification, the model is based on a laminar Schmidt number, of high value (as previously explained, an infinite Schmidt number is chosen). This is consistent with the following results showing that the key parameters are situated at the inflection point. However, during the development of shear instability and the non-linear transition of this interfacial layer to turbulence, the direct numerical simulation code will reproduce a mixing by eddies, leading to an effective Schmidt number in this region of the order of the unity, reproduced by simulations. The main contribution of the upper layer is to inject some perturbations into the region of the shear layer which is the laminar zone around the inflection point. This effect is implicitly taken into account in the present evolution of the interface.

In the following, we choose as a reference case $\lambda = 0.1$ and $4\,\delta/\sqrt{\pi} = 0.3$ m. A no-slip (resp. free-slip) condition is imposed for the velocity at the bottom (resp. top) boundary while zero normal gradient is imposed for ϕ. Periodic boundary conditions are imposed along the streamwise direction. A zoom of the corresponding profiles for $\bar{u}(z)$, $\bar{\rho}(z)$ and $\bar{\mu}(z)$ is displayed in figure 2.

With the present assumptions, the flow is described by four dimensionless parameters, namely,

$$At = \frac{\rho_2 - \rho_1}{\rho_2 + \rho_1}, \quad Re = \frac{4\,\delta}{\sqrt{\pi}}\,u_h\,\frac{\rho_h}{\mu_h}, \quad Ri = 2\,\delta\,\frac{g}{\rho_h}\,\frac{(\rho_2 - \rho_1)}{(u_2 - u_1)^2}, \quad W = \log_{10}\left(\frac{\mu_1}{\mu_2}\right), \quad (7)$$

where $u_h = \bar{u}(h)$, $\rho_h = \bar{\rho}(h) = (\rho_2 - \rho_1)\lambda + \rho_1$ and $\mu_h = \bar{\mu}(h) = (\mu_2 - \mu_1)\lambda + \mu_1$ are respectively the velocity, the density and the viscosity of the fluid at the interface $z = h$. The Reynolds number Re and the gradient Richardson number Ri are computed at the location of maximum density gradient, i.e. at the interface. The viscosity ratio between mud flow and water is expressed by its decimal logarithm W. Excepted otherwise mentioned, the Atwood number is fixed to $At = 0.15$ in this study and the Reynolds number ranges in $Re \in [1, 10^6]$. It is important to note that the chosen Reynolds number is computed at the inflection point, in the interface layer, and so principally depends on mud viscosity. With this choice, the value of this interfacial Reynolds number is lower than the corresponding Reynolds number based on the velocity of the less viscous region. In addition, only the initial linear development of the instability was simulated for the largest Reynolds numbers investigated here, namely $Re = 10^5$ and 10^6 because of the limited spatial resolution of the present Navier-Stokes simulations. Since we focus on instabilities,

the Richardson number will be varied in a range $Ri \in [0, 0.3]$. The dimensionless number W varies from 0 to 3, which corresponds to a viscosity ratio varying from 1 to 10^3. This present range of parameters can be view as taking $\rho_{water} = \rho_2 = 1000$ kg.m^{-3} and $\mu_{water} = \mu_2 = 10^{-3}$ Pa.s, a concentration in the range [0, 580] g.l^{-1} corresponding to a range of density [0, 1360] kg.m^{-3} and viscosity [10^{-3}, 1] Pa.s and a characteristic velocity in the range $[0, 2.5]$ m.s^{-1}. These values are typical of what is measured in estuaries (Hardisty, 2007).

2.3 Description of the two numerical approaches

2.3.1 Linear stability solver

The linear stability code LiSa, developed by Antkowiak and Brancher (2007), is used to obtain a global vision of the problem. This code solves the system (1-3) linearized around the base flow given by Equation (6). Given such a parallel base flow and fixed values for the control parameters and the horizontal wavelength, LiSa computes the eigenvalues and their associated modes. The matrices to diagonalize are built through a spectral method based on a Chebyshev polynomial decomposition of the fields in the vertical direction. Therefore, one can extract from the spectrum the most unstable mode and its growth rate. Two versions of the code are used. The first one relies on a real mapping between the Gauss-Lobatto grid points and the physical domain, developed for this specific problem. The second version, following the idea of Fabre et al (2006), uses a complex mapping between the physical and spectral spaces that allows to improve the numerical convergence for the eigenvalues in some configurations (see Appendix for more detail).

2.3.2 Navier-Stokes solver

The JADIM code, developed at IMFT (Institut de Mécanique des Fluides de Toulouse), solves the Navier-Stokes equations (1-3) for variable-density, variable-viscosity and incompressible flows. Equations for the primitive fields (velocity, pressure) are solved by a finite-volume method. The code is second order accurate in space and time (Calmet and Magnaudet, 1997; Legendre and Magnaudet, 1998). A third order Runge-Kutta temporal scheme is combined to a semi-implicit Crank-Nicolson scheme for diffusive terms. The equations are discretized using second-order centered differences with staggered variables. The transport equation of the volume fraction is discretized using a WENO (Weighted Essentially Non Oscillatory) scheme (Jiang and Shu, 1996). The present version of the solver has been validated for a viscosity gradient by Bonometti et al (2008) and for a density gradient by Hallez and Magnaudet (2009) in a context of gravity currents. As Bonometti et al (2008) use a FCT (Flux Corrected Transport) scheme and Hallez and Magnaudet (2009) a centered scheme for transport equation of the volume fraction, the choice of a WENO scheme is justified by coexistence in our configuration of smooth and steep gradients. This choice allows for both stability of the scheme and accurate transport of the volume fraction.

3 Linear development of the instability

3.1 Notations for the temporal stability analysis

Linear stability analyses are performed by linearizing Equations (1-3) around the general base flows $\bar{u}(z)$ and $\bar{\phi}(z)$ defined at the beginning of Section 2.2. Because of the invariance of the system with time, streamwise and spanwise directions, small perturbations are sought as superpositions of modes of the form:

$$\mathbf{A}(x, y, z, t) = \mathbf{a}(z)\, e^{i(kx+\beta y)} e^{\sigma t - i\omega t} \, ,$$

where $\mathbf{A} = (\hat{u}, \hat{v}, \hat{w}, \hat{p}, \hat{\phi})$ is the perturbation field, k and β the wavenumbers in the streamwise and spanwise directions, ω the frequency and σ the growth rate and $\mathbf{a}(z)$ an unknown vectorial profile. Perturbations are represented by the velocity field $(\hat{u}, \hat{v}, \hat{w})$, the pressure $\hat{p}$, the density $\hat{\rho}$ and the viscosity $\hat{\mu}$.

In the following, normalization is performed with $(u_2 - u_1)/2$ for velocity units and δ for length units. The wave vector is then normalized as $k^* = k\,\delta$ and $\beta^* = \beta\,\delta$, the frequency as $\omega^* = 2\,\omega\,\delta/(u_2 - u_1)$, the growth rate as $\sigma^* = 2\,\sigma\,\delta/(u_2 - u_1)$ and the time as $t^* = 2\,t\,\delta/(u_2 - u_1)$.

3.2 LiSa validation and series of profiles

The linear stability code LiSa has been first validated on the case of an inviscid and density stratified shear flow in an unbounded domain.

For this validation, we refer to Hazel (1972) who considers the following profiles: $\bar{u} = u_0 \tanh(z/\delta)$ and $\bar{\rho} = \rho_0 \exp[-At \tanh(z/\delta)]$ under the Boussinesq approximation. Here, we consider instead $\bar{u} = u_0 + u_0 \tanh(z/\delta)$ which does not change the temporal stability analysis, except for a shift in the phase velocity. We choose a small Atwood number ($At = 0.024$) in order to approximate the density profile by $\bar{\rho} \sim \rho_0[1 - At \tanh(z/\delta)]$. Since Hazel (1972) focuses on inviscid fluid, we choose a small viscosity value $\mu = 10^{-3}$ Pa.s that leads to $Re \sim 3\,10^5$. The choice $u_0 \sim 1$ m.s^{-1} (varying with Ri) and $\rho_0 = 1000$ kg.m^{-3} is arbitrary since only the dimensionless numbers are considered for this validation.

	$Ri = 0.01$	$Ri = 0.05$	$Ri = 0.1$	$Ri = 0.15$	$Ri = 0.2$
Hazel (1972)	0.1838	0.1594	0.1259	0.0889	0.0472
LiSa code	0.1838	0.1593	0.1259	0.0889	0.0471

Table 1: Maximum normalized growth rate σ^* for various Richardson numbers Ri. The results of Hazel (1972) are compared to the results of the linear stability code LiSa for $At = 0.024$.

Table 1 presents a validation on the maximum growth rate for different Richardson numbers in the case of unbounded boundary conditions. The results are consistent with Hazel (1972), up to the precision of the numerical method.
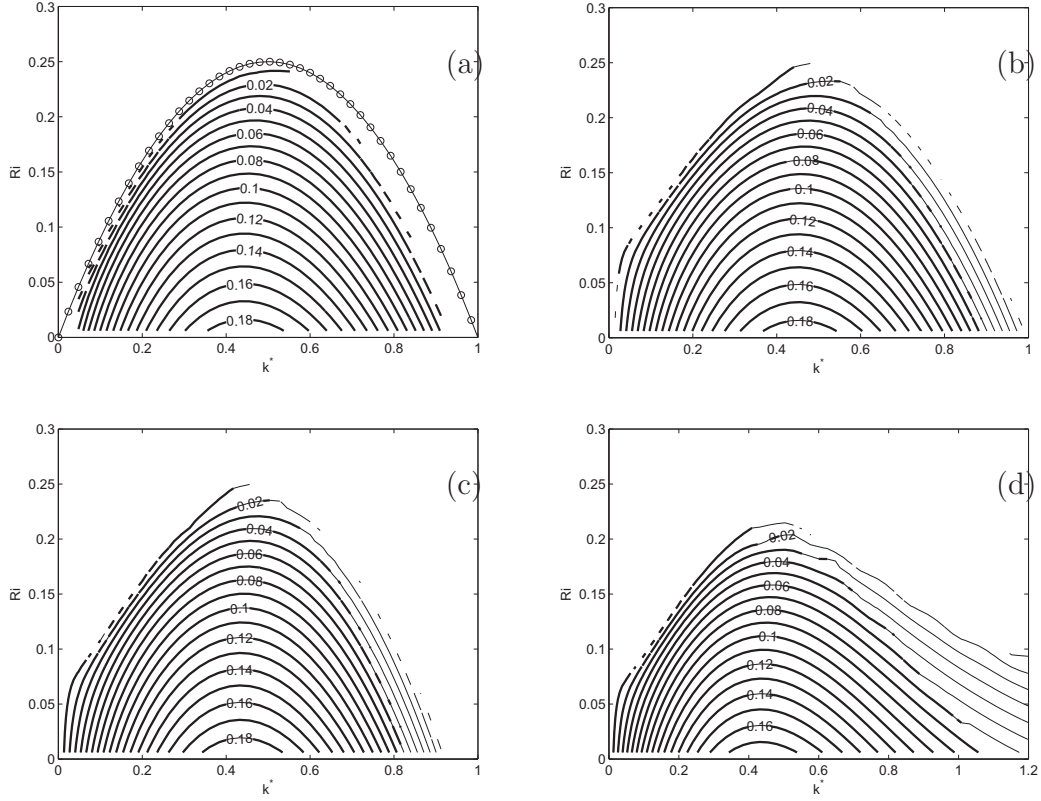
Figure 3: Isocontours of the growth rate σ^* as a function of k^* and Ri for high Reynolds numbers. (a) Hazel (1972)'s tanh profiles with vanishing boundary conditions at infinity, (b) tanh profiles in a bounded domain, (c) symmetric erf profiles in a bounded domain, (d) asymmetric erf profiles in a bounded domain. Line with circles: theoretical neutral curve, bold line: real mapping, thin line: complex mapping; only converged eigenvalues are shown.

The other growth rates are shown on Figure 3(a) as a function of the wavenumber k^* and the Richardson number Ri (iso-contours are interpolated from a 50×50 grid in this diagram). Only converged eigenvalues are represented, which explains lack of eigenvalues at some locations. The thin parabolic line with circles in Figure 3(a) described by the equation $Ri = k^*(1-k^*)$ represents the neutral curve (Hazel, 1972). Good agreement on this case is observed in spite of some expected difficulties to access the low growth rates, particularly for large wavenumbers.

Starting with the Hazel's configuration (Figure 3(a)), we have then considered a progressive transition (Figures 3(b) and 3(c)) towards our reference case with asymmetric erf functions (Figure 3(d)). For these new cases (b, c and d), the Bousinesq approximation is no longer used and the Atwood number is set to $At = 0.15$. The Reynolds number is set to $Re \sim 5\,10^5$. For all cases of Figure 3, the iso-contours that are represented with bold lines are obtained with a distribution of spatial grid points obtained with a classical mapping ("real mapping", see Appendix). The part represented with thin lines has been computed with a different mapping ("complex mapping", see Appendix), in which the coordinates of the grid points lie in the complex plane.

Figure 3(b) deals with tanh profiles in a bottom no-slip and top free-slip bounded domain described in Section 2.2. We have noticed that replacing no-slip by free-slip boundary conditions at the bottom led to no visible difference in the results. In agreement with Hazel (1972), confining the flow increases the growth rate for small wavenumbers and only the large waves are "aware" of the presence of the boundary. On Figure 3(c), the base function is changed from tanh to erf. The modification of the sharpness of the interface acts on higher wavenumbers. The marginal curve is no longer parabolic and does not pass through wavenumber $k^* = 1$. Finally, Figure 3(d) presents our reference study case as introduced at the end of Section 2.2. This configuration corresponds to an asymmetric erf function at the interface for which the asymmetry parameter is fixed to $\lambda = 0.1$ and the viscosity is homogenous ($W = 0$). In this case, the asymmetry of the interface increases the growth rate at large wavenumbers.

3.3 Characterization of the stability of the interface

We now focus on the reference erf profile case with $\lambda = 0.1$ and densities fixed to $\rho_1 = 1360$ kg.m^{-3} and $\rho_2 = 1000$ kg.m^{-3}, corresponding to an Atwood number $At = 0.15$. No-slip (resp. free-slip) boundary conditions at the bottom (resp. top) of the $z \in [0, H]$ domain with $H = 3$ m are considered. The interface lies at $h = 1$ m and "inflection point thickness" is such that $4\,\delta/\sqrt{\pi} = 0.3$ m. Since $u_1/u_2 \ll 1$, the variations of the Richardson number Ri, the Reynolds number Re and the viscosity ratio W only trace back the variations of the velocity u_2 and the viscosities μ_1 and μ_2.

For homogeneous flows, the Squire theorem (Squire, 1933) ensures that the most unstable perturbations first appear as 2D modes ($\beta = 0$). Since such a theoretical result does not exist for the present stratified flow, we have performed an exploration of 3D configurations that suggests that this might be also the case here (see
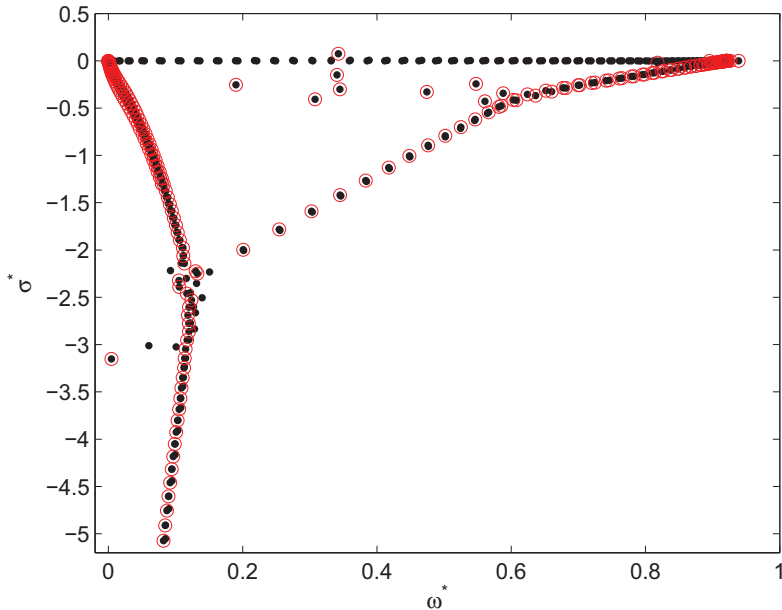
11

Figure 4: Eigenvalues spectrum in the plane (ω^*, σ^*) for $Re = 10^2$, $Ri = 0.15$, $W = 3$ and $k^* = 0.46$. The circles correspond to converged eigenvalues.

Section 4.3). For this reason, we restrict the present study to 2D perturbations.

A typical spectrum of eigenvalues computed with LiSa is displayed in Figure 4 for a particular set of parameters. The vertical structure of the most unstable eigenmode are displayed in Figure 5. The influence of the base flow asymmetry, introduced by the parameter λ, is observed on the structure of the mode. The instability is not located on the inflection point of the profile at $z = h = 1$ m, as it would be the case for $\lambda = 0.5$, but a little higher at $z = 1.07$ m. Asymmetry also leads to a stretching of the modes above the interface and a contraction below.

These modes have been compared to modes obtained with a smaller and no viscosity ratio between fluids, for a constant Reynolds number at the interface. The viscosity ratio has only a small influence on the vertical position or the general shape of the modes. For pressure and density, the viscosity ratio slightly increases the amplitude of perturbation profiles. For velocities, the increase of the viscosity ratio slightly decreases the amplitudes of perturbation under the interface where the fluid viscosity is increased, and increases these amplitudes over the interface where viscosity is decreased. These variations between different viscosity ratios are small (less than 10%).

3.4 Parameters sensitivity

The dependency of the growth rate σ^* at $Re = 10^2$ with the Richardson number is displayed on Figure 6 for $W = 3$. Bold and thin lines correspond respectively to the real and complex mappings as described for Figure 3. As pointed out in the previous
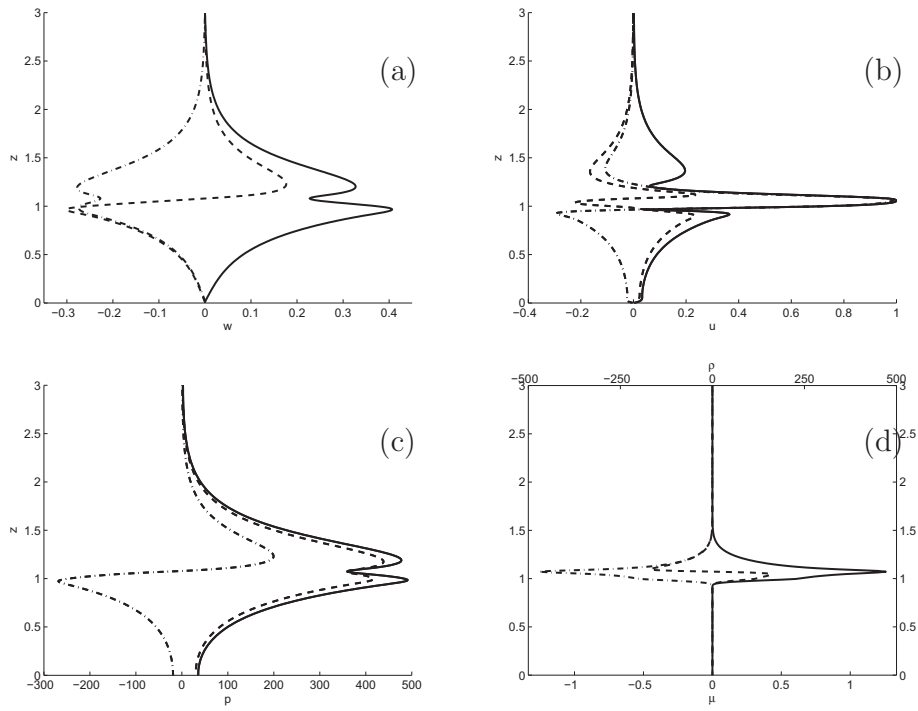
12

Figure 5: Vertical profiles of the most unstable mode at $Re = 10^2$, $Ri = 0.15$, $W = 3$ and $k* = 0.46$ for: (a) vertical velocity, (b) streamwise velocity, (c) pressure and (d) density, normalized by the maximum of the streamwise perturbation. Dashed - - : real part. Dotted-dashed -·- : imaginary part. Plain - : absolute value.
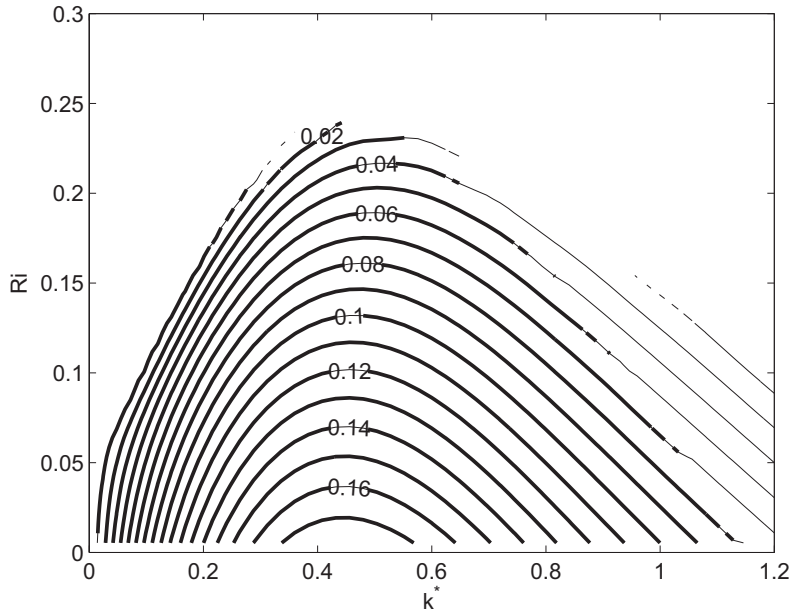
Figure 6: Isolines of the normalized growth rate σ^*, as a function of the non-dimensional wavenumber k^* and the Richardson number Ri for $W = 3$ and $Re = 10^2$.

section, the increase in the growth rate observed for small wavenumbers comes from confinement. Increasing profiles asymmetry at the interface implies a larger range of unstable wavenumbers for large wavenumbers. Smaller wavelengths are destabilized by the sharper gradient in the lower part of the interface, their characteristic length being $\lambda\delta$. Figure 7, which shows isocontours of the growth rates for $W = 3$ in the wavenumber and Reynolds number plane, illustrates the influence of the Reynolds number. For Reynolds number higher than 10^3, the growth rate no longer depends on the viscosity, which is a known feature of KH instabilities. But for Reynolds numbers smaller than this value, we observe a greater growth rate accompanied by a larger interval of unstable wavenumbers: the viscosity has a destabilizing influence. On Figure 8, isocontours of the growth rate for different viscosity ratios W are presented. At first, a good correlation between the curves is observed, prooving the relevance of the chosen definition of the Reynolds number. For Reynolds numbers higher than 10^3, the growth rate does not depend on the viscosity ratio, which is consistent with the fact that the stability properties are independent of viscosity at high Reynolds numbers. To illustrate the small Reynolds number features, a section of this diagram at $Re = 10^2$ is shown on Figure 9. We can note that a larger viscosity ratio between fluids increases this destabilizing effect previously observed for viscosity. Figure 10, which represents the evolution of the maximum KH growth rate with respect to Reynolds number, clearly shows that viscosity stratification changes the location of the initial instability. It also suggests a lower critical Reynolds (of $O(10)$) for the development of the instability for large viscosity ratios.

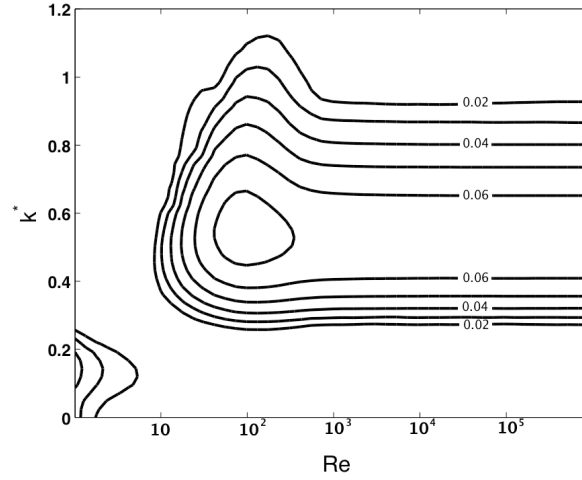On Figures 7 and 8, one can notice an instability of different nature for low Reynolds

14

Figure 7: Isocontours of the normalized growth rate σ^*, as a function of the non-dimensional wavenumber k^* and the Reynolds number Re for $Ri = 0.15$ and $W = 3$.

numbers and low wavenumbers. As in Yih (1967), we observe a long wave instability in the present case of two layers of fluids with the thinnest being the most viscous. Recent work of Govindarajan (2004) on concentric pipe flow of miscible fluid of different viscosities presents similar results. The mode observed in our configuration might be the "overlap" mode, a deformation of the Tollmien-Schlichting mode developing in a variable viscosity region, close to the Yih mode observed for immiscible interfaces. Since we focus on the KH instability, no further investigation of this instability is presented here.
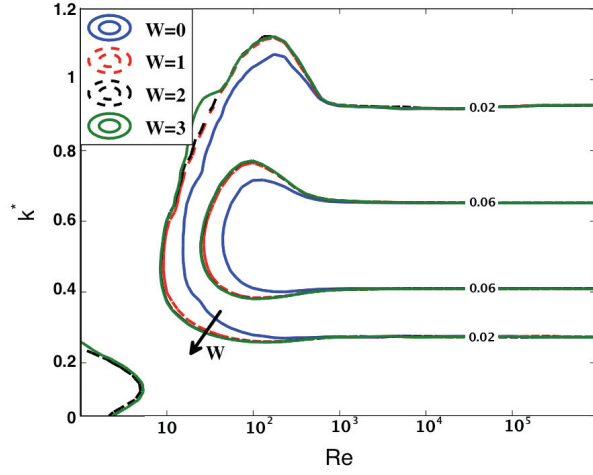
Figure 8: Isocontours of the normalized growth rate σ^*, as function of the non-dimensional wavenumber k^* and the Reynolds number Re, for $Ri = 0.15$ and for $W \in \{0, 1, 2, 3\}$.
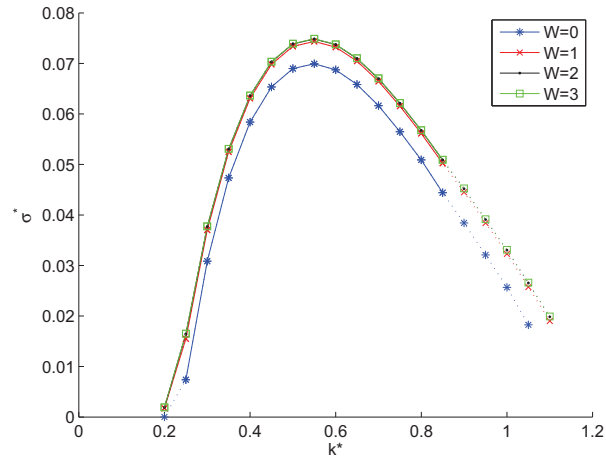

Figure 9: Normalized growth rate σ^* as function of the non-dimensional wavenumber k^*, for $Ri = 0.15$, $Re = 10^2$ and $W \in \{0, 1, 2, 3\}$.
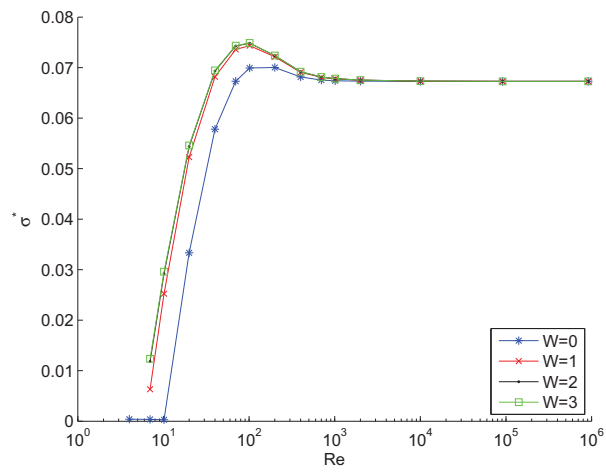
16

Figure 10: Maximum growth rates as functions of the Reynolds number at $Ri = 0.15$ and for $W \in \{0, 1, 2, 3\}$.

4 Non-linear evolution of the instability

The linear stability analysis of the previous section is now complemented with direct numerical simulations (DNS). The velocity, density and viscosity fields of the most unstable mode are used to initialize 2D simulations in a streamwise periodic domain. The nonlinear regime subsequent to the linear growth is investigated.

4.1 Preliminary comparison between Navier-Stokes simulations and linear stability results

We first focus on the linear growth, i.e. the first stage of development of the instability. We choose $k_* = 0.46$, which leads to a x-period $L = 2\pi/k \sim 1.8$ m since $k = k_*/\delta$ and $\delta = 0.3\sqrt{\pi}/4$. The mesh size is fixed to 0.5 cm × 0.5 cm, which corresponds to a (x, z)-resolution of 364×600. In Figure 11 is represented the kinetic energy of velocity perturbations computed from the velocity perturbations $\hat{\mathbf{u}} = \mathbf{u} - <\mathbf{u}>_x$ through

$$||\hat{\mathbf{u}}||^2 = \frac{1}{HL} \int_0^H \int_0^L \left[(u - <u>_x)^2 + (v - <v>_x)^2 \right] dx\, dy, \qquad (8)$$

where $<>_x$ represent space average in the x direction. The choice to subtract the mean flow computed at the given time, instead of subtracting the initial mean flow, avoid to take into account diffusion of the mean flow in the amplitude of perturbations. Various Reynolds numbers were investigated in order to assess the sensibility of this parameter on the instability growth rate. At early times ($t^* \leq 15$), the growth of $||\hat{\mathbf{u}}||^2$ is exponential and independent of Re. This is in agreement with the linear stability results, which predict the growth rate σ^* to be independent of Re for $Re \geq 10^3$ (Figure 10). At longer times ($15 \leq t^* \leq 50$), the growth rate of the instability still follows an exponential trend at $Re \geq 10^3$ while at lower Re, the kinetic energy is significantly lower by an order of magnitude, approximately. At long times ($t^* \geq 50$), the kinetic energy of the perturbations saturates and oscillates around a plateau value at 10^{-2} for $Re \geq 10^3$ and 10^{-3} for $Re = 10^2$. The growth rates obtained from the direct numerical simulations of the linear stability analysis are presented in Table 2. As expected, when the Reynolds number Re increases, the dependency with W is no longer visible. For large Reynolds numbers, the viscosity ratio has no influence on the development of the primary instability again in agreement with the linear stability analysis results (see e.g. Figure 10). A quantitative agreement is observed with linear stability results, the differences being less than 1% for $Re \geq 10^4$. This indicates that, with the present resolution, the Navier-Stokes solver is able to accurately capture the instability of the mixing layer within the investigated range of parameters.

For low Reynolds numbers, the Navier-Stokes simulations slightly differ from the linear stability predictions because the hypothesis of a quasi-steady base flow is no longer valid. A characteristic time of the instability, based on growth rate, is $\tau_{inst} = \frac{2\delta}{\sigma^*(u_2 - u_1)}$ while a characteristic time for base flow diffusion is $\tau_\nu = \frac{(\lambda\delta)^2 \rho_h}{\mu_h}$.

18

Growth rate σ^*		$Re = 10^2$	$Re = 10^3$	$Re = 10^4$	$Re = 10^5$	$Re = 10^6$
$W = 0$	Linear stability	0.5688	0.5532	0.5521	0.5520	0.5520
	DNS	$\times$	0.5039	0.5485	0.5509	0.5511
$W = 3$	Linear stability	0.6098	0.5567	0.5525	0.5521	0.5520
	DNS	0.5848	0.5482	0.5504	0.5507	0.5500

Table 2: Normalized growth rate σ^* for various Reynolds numbers Re and viscosity ratios W ($Ri = 0.15$ and $k^* = 0.46$), obtained from DNS and compared with the linear stability analysis.

The ratio between those characteristic times is:

$$\frac{\tau_{inst}}{\tau_\nu} = \frac{2\,\delta}{\sigma^*(u_2 - u_1)} \frac{\mu_h}{(\lambda\delta)^2\rho_h} = \frac{1}{Re} \frac{8}{\sqrt{\pi}\lambda\sigma^*}.$$

$\tau_{inst}/\tau_\nu \sim 0.9$ for $Re = 100$, which means that the mean flows diffuses on a time scale comparable to the one of the instability development. Contrary to the higher Re regimes, the base flow can no longer be considered as steady during the development of the instability. Therefore, the growth rate of the perturbation is exponential only during a short times and is rapidly impeded by the diffusion of the base flow long before the non-linear saturation observed for high Reynolds numbers occurs. Note that at the end of linear growth, the streamwise-averaged density profile was observed to be quasi-steady for all Re while the streamwise-averaged velocity profile kept diffusing in regions where gradients are large for $Re \leq O(10^2)$ (not shown here).

4.2 Saturation and non-linear evolution of the instability

The subsequent stages of the evolution of the instability are described in this section. To highlight the influence of both viscosity and density stratifications, the reference case $Re = 10^3$, $Ri = 0.15$ and $W = 2$ is compared to the $W = 0$ case in which the viscosity stratification is removed and the $Ri = 0.05$ in which the density stratification is decreased. The length of the simulation box is now $L = 4 \times 2\pi/k$, corresponding to four spatial wavelengths of the instability ($L = 7.263$ m) in our configuration where $k^* = 0.46$.

The simulations are realized on a 1496×600 mesh, which is refined near the interface: vertical grid size $d_z/h = 0.25\ 10^{-3}$ for $0.75 \leq z/h \leq 1.5$. In the regions $0 \leq z/h \leq 0.75$ and $1.5 \leq z/h \leq 3$, d_z varies linearly from $d_z/h = 2.5\ 10^{-3}$ close to the interface to $d_z/h = 1.25\ 10^{-2}$ at the top and bottom boundaries. We define the mixing layer thickness Δ by :

$$\Delta(t) = \frac{1}{h} \int_0^H \frac{<\rho u>_x}{(\rho_2 - \rho_1)(u_2 - u_1)} \left[1 - \frac{<u>_x}{(u_2 - u_1)}\right] dz.$$

The temporal evolution of Δ is displayed in Figure 12, for the reference case together with a case of no viscosity (weak density) stratification, i.e. $W = 0$ ($Ri = 0.05$). In
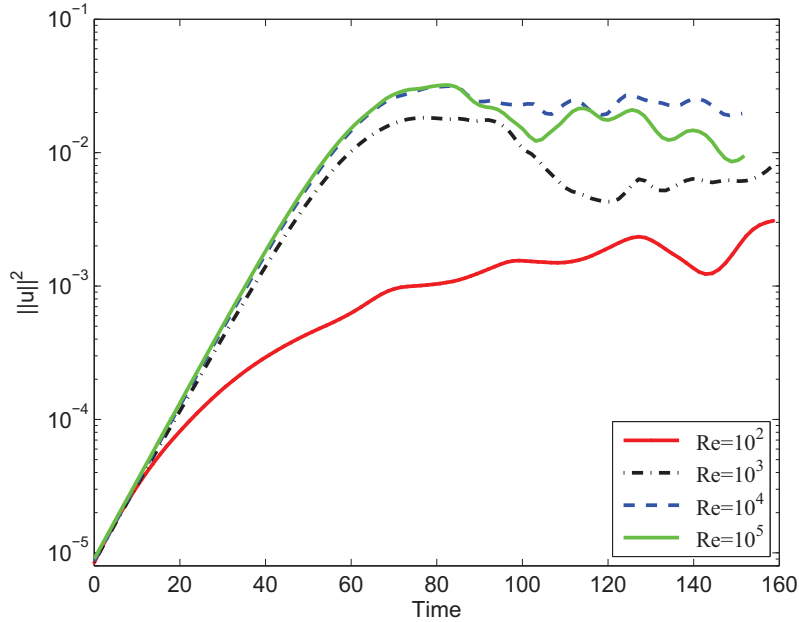
19

Figure 11: Time evolution of the perturbation kinetic energy ($\|\hat{\mathbf{u}}\|^2$) for $W = 3$, $Ri = 0.15$, $k^* = 0.46$ and $Re = 10^2$, 10^3, 10^4 and 10^5. Time being normalized as $t^* = 2\, t\, \delta/(u_2 - u_1)$.

all cases, the temporal evolution of the mixing layer thickness is not monotonous but is characterized by a succession of plateaus and rapid growths, which are sometimes followed by a peak. As described later, these peaks are observed during vortex pairing phenomenon.

Keeping in mind that the evolution of the interface is constrained by the periodicity of the simulation domain, we can relate the evolution of $\Delta(t)$ to the structure of the flow. For this purpose, circles of Figure 12 correspond to the times at which density and vorticity fields are extracted for the whole domain and plotted in Figure 13 and Figure 14, vorticity being normalized by u_h/δ. At $t^* \sim 73$ (fig. 13(a)), the KH rolls reach their maximum of amplitude. Contrarily to non-stratified configurations, positive vorticity is observed. This vorticity is created by the baroclinic torque, associated to strong density gradients and the vorticity fields (see Staquet, 1995). The KH rolls destabilize through an elongation of vorticity braids between the vortices (Figure 13(b-c)). The braids break up while the vortices are still coherent. This secondary instability, of the "near-core" type (see Staquet, 1995), consists in the destabilization by a jet (Figure 13(c) left) near the core of the vortex, leading to the break up of the braid. This destabilization is followed by the generation of small vortices (Figure 13(d)). This evolution significantly differs from the case of more viscous flows, for which the development of sub-harmonics and subsequent pairing is observed without deformation nor breaking of the vorticity braid (not show here). The flow is then disorganized with secondary vortices located on the border of the mixing layer. They are located at a maximum of vorticity, which is more intense
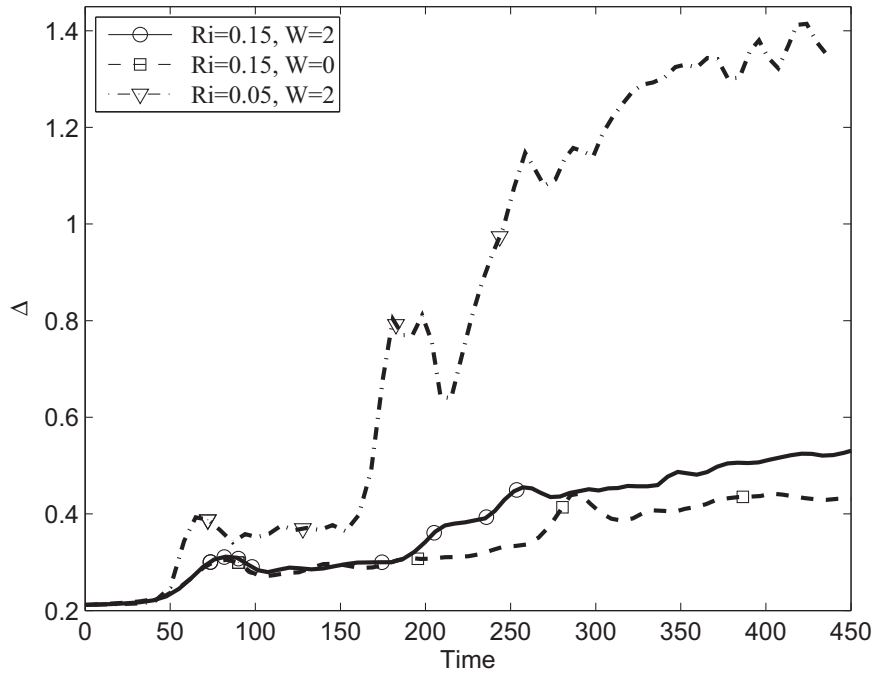
20

Figure 12: Time evolution of the mixing layer thickness $\Delta(t)$. Results obtained from direct numerical simulations for $Re = 10^3$. The symbols correspond to the different instants of the density and vorticity fields displayed in figures 13 to 16. Time being normalized as $t^* = 2\,t\,\delta/(u_2 - u_1)$.
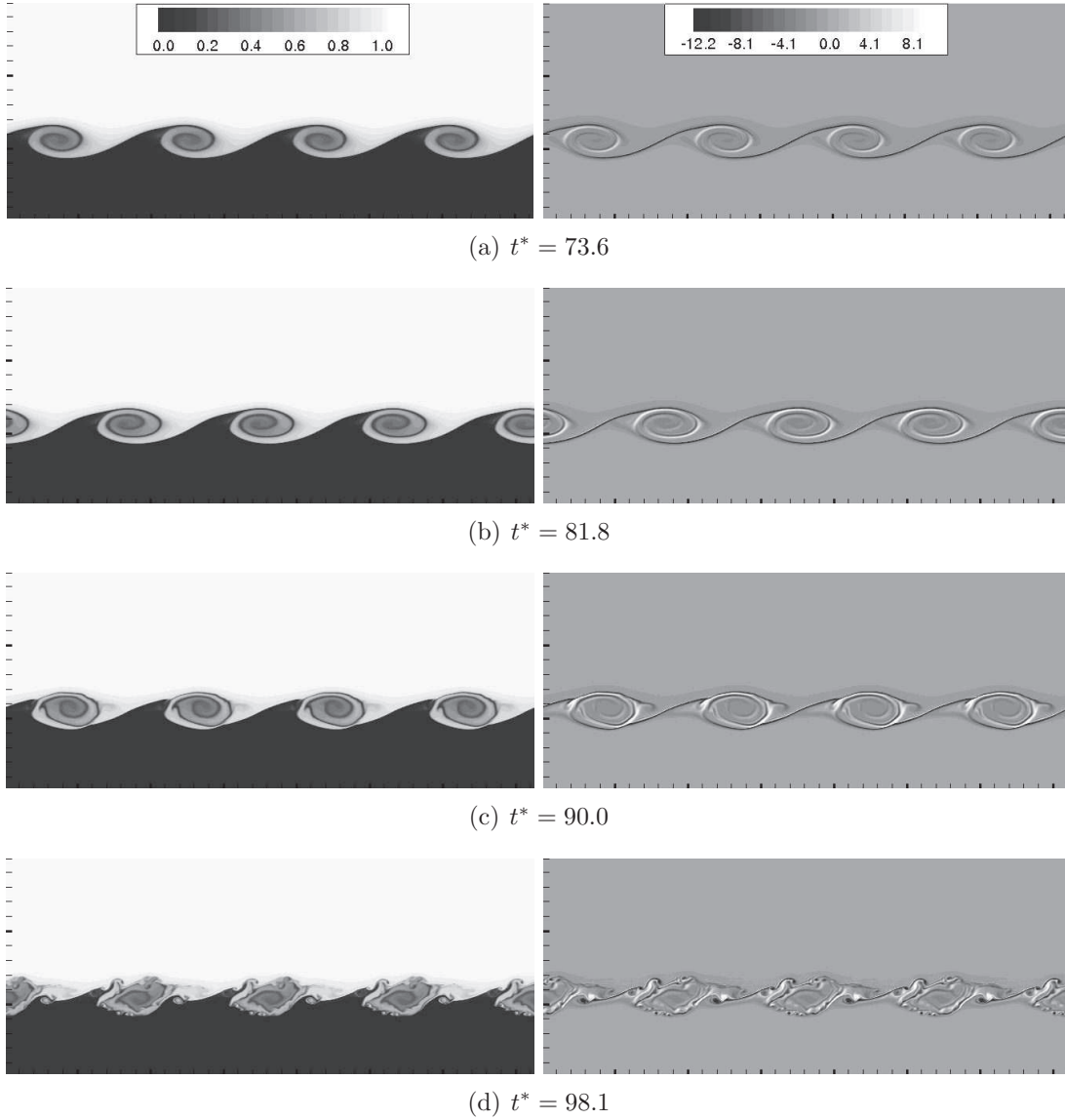
(a) $t^* = 73.6$

(b) $t^* = 81.8$

(c) $t^* = 90.0$

(d) $t^* = 98.1$

Figure 13: Temporal evolution of KH rolls for $W = 2$, $Ri = 0.15$ and $Re = 10^3$, $70 \leq t^* \leq 100$. Left: density, right: spanwise vorticity. The whole computational domain is shown.

22

on the perimeter of the primary KH eddies. Some of the energy is transferred to small lengthscales and then dissipated by diffusion. At later times ($t^* \geq 150$), the flow reorganizes and the main eddies move toward the center of the mixing layer: at $t^* \sim 174$ (Figure 14(a)), a dark patch of vorticity appears inside the layer. At this stage, the flow is still composed of four main structures reminiscent of the initial KH rolls and the thickness of mixing layer has not changed since the end of the linear growth (Figure 12). Then pairing, or coalescence, occurs: vortices roll around each other and mix to form larger structures. At $t^* \sim 205$ (Figure 14(b)), on the left part of vorticity field cartoon, three eddies are clearly seen and begin to roll-up around each other to form a bigger eddy. On the right side, two others begin the process of pairing. This stage corresponds to the thickening of the interface observed on Figure 12 (see the circle at time $t^* = 205.1$). Finally at $t^* \sim 236$ (Figure 14(c)), only three main vortices are present. One pairing has ended while the other are still going on. During this stage, the thickness of the mixing layer is constant. At $t^* \sim 254$ (Figure 14(d)), a second pairing (in the center of the figures) is ending.

The comparison of the evolution of the mixing layer with the other configurations, namely no-viscosity stratification and weak density stratification, give indications on the influence of the two stratifications. The density stratification, represented by the Richardson number, is observed to be very influent on the thickness of the interface (Figure 12). For instance, at $t^* \sim 150$ (resp. 400), the thickness of the mixing layer is about 30% (resp. 300%) larger in the weak density stratification case ($\Delta \sim 0.3$ (0.4) at $t^* \sim 150$ and $\Delta \sim 0.4$ (1.4) at $t^* \sim 400$, for $Ri = 0.15$ (0.05)). As shown in §3, decreasing the Richardson number decreases the impact of the stratification on the development of primary instability and leads to an increase of the growth rate and eventually to a thicker mixing layer. This is in agreement with the present observations. The viscosity stratification does not affect the thickness of the mixing layer at early times ($t^* \leq 160$) while it slightly increases Δ at later times ($t^* > 160$) by about 20%, after vortex pairing has occurred. In both $Ri = 0.15$ and $Ri = 0.05$ cases, the saturation of primary instability is followed by the development of small vortices and a reorganization of the interface. After a time period that is equivalent for both cases, a first stage of coalescence, rapidly followed by a second stage, are observed. In the $Ri = 0.05$ case, the development of the second pairing is hampered by the size of the simulation box (Figure 15(c-d)).

The comparison between the two $Ri = 0.15$ simulations with $W = 2$ and $W = 0$ (homogeneous viscosity) traces back the influence of viscosity stratification. The development of the primary instability is not influenced by the viscosity stratification, nor is the secondary instability (Figure 16(a) and Figure 13(c)). However, the viscosity stratification has an influence on the pairing. While a first pairing is observed at $t^* \sim 280$ (Figure 16(c)) for $W = 0$, with no subsequent coalescences, for $W = 2$, the first pairing is observed at $t^* \sim 200$ and is followed by a new pairing at $t^* \sim 250$ (Figure 14(d)), these pairings presenting different morphologies. This faster sequence of pairings, enhanced by the viscosity stratification, widens the interface. Eventually, the thickness of the mixing layer in the viscous-stratified flow is 20% thicker than in the uniform viscosity case. This present results confirm that density and viscosity stratification can have a significant influence on the non-
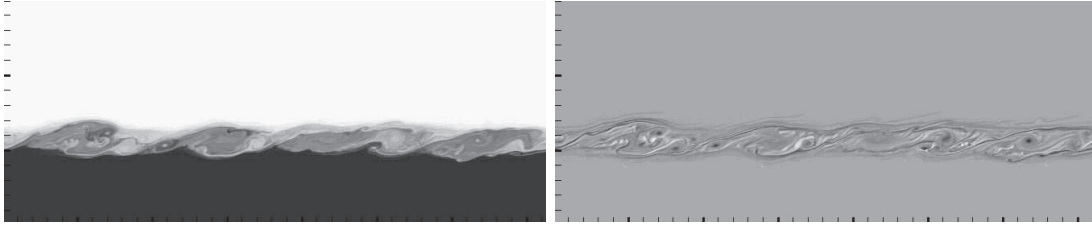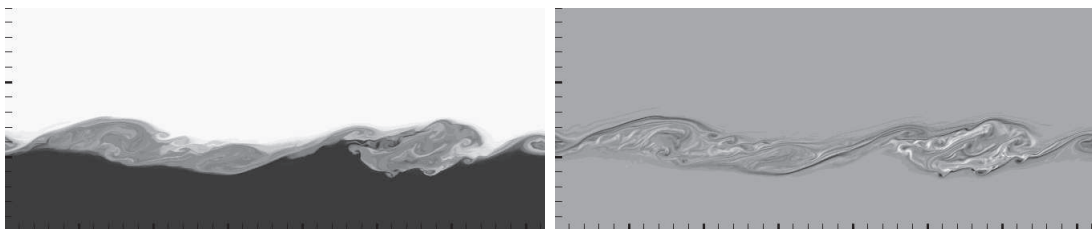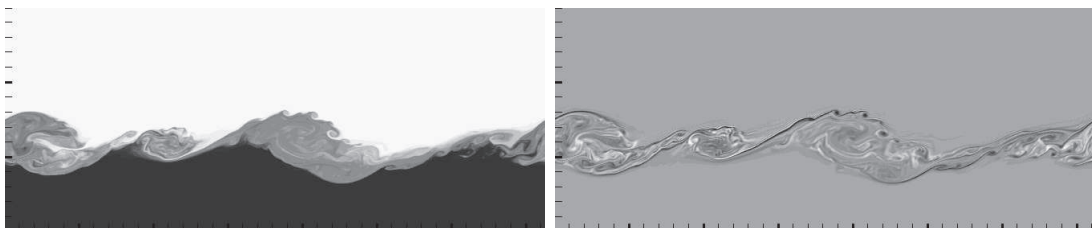
(a) $t^* = 174.4$
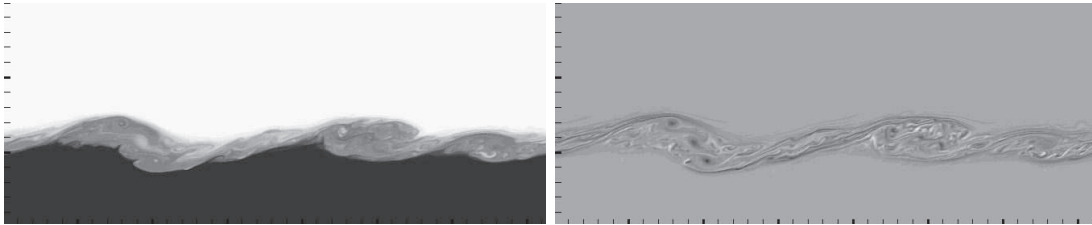
(b) $t^* = 205.1$

(c) $t^* = 235.8$

(d) $t^* = 253.6$

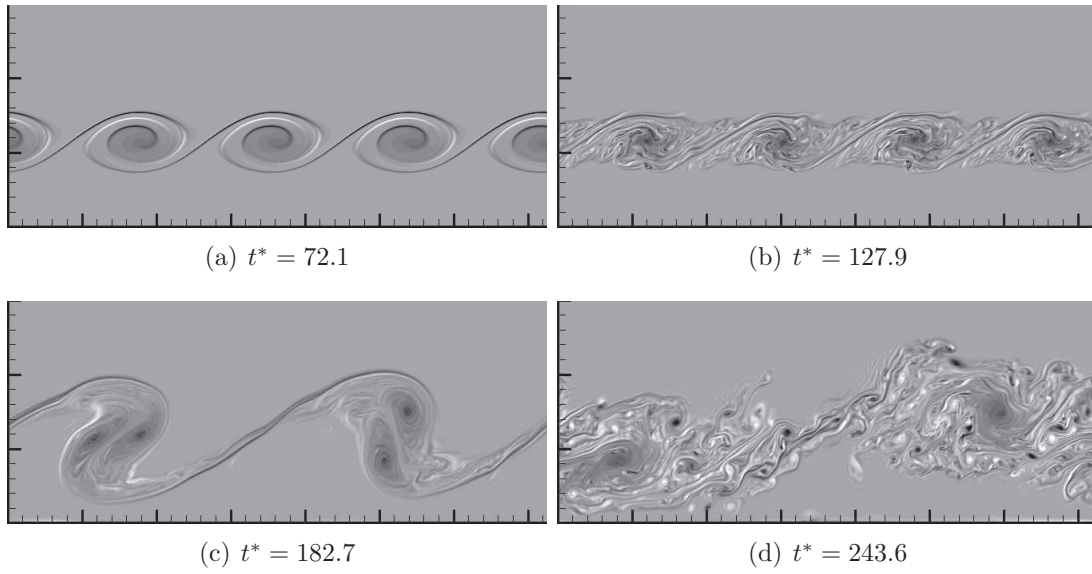Figure 14: Same as in figure 13 for later times $150 \leq t^* \leq 300$.

(a) $t^* = 72.1$

(b) $t^* = 127.9$

(c) $t^* = 182.7$

(d) $t^* = 243.6$

Figure 15: Temporal evolution of vorticity field of KH rolls for $W = 2$, $Ri = 0.05$ and $Re = 10^3$. Vorticity being normalized by u_h/δ and presenting the same color-bar as Fig. 13.

linear development of the mixing layer, thus modifying the thickness of the interface accordingly.
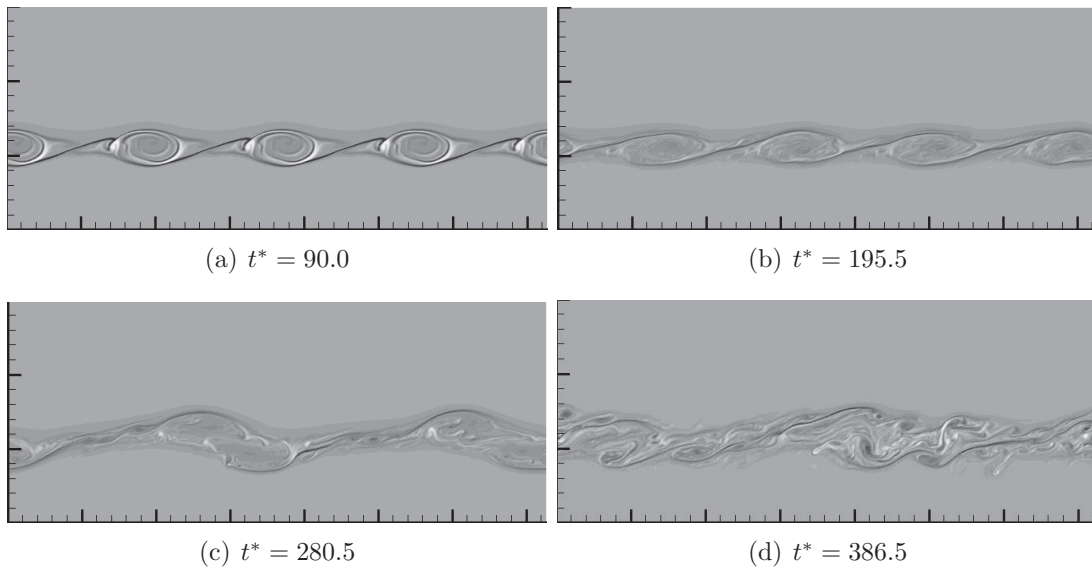
(a) $t^* = 90.0$

(b) $t^* = 195.5$

(c) $t^* = 280.5$

(d) $t^* = 386.5$

Figure 16: Same as in figure 15 for $W = 0$, $Ri = 0.15$ and $Re = 10^3$

4.3 On three-dimensionalisation

In the case of inviscid flows, Squire (1933) has demonstrated that, given a three-dimensional unstable mode, there exists at least one two-dimensional mode that is more unstable. This theorem has been generalized to viscous flow (Yih (1955)) as follows: given an unstable oblique mode, one can find a more unstable two-dimensional mode at a lower Reynolds number. Therefore, the critical Reynolds number can be determined considering only 2D-modes. Nevertheless, it is not demonstrated that for a given unstable Reynolds number, the most unstable mode will be two-dimensional (see examples in Caulfield (1994) regarding Holmboe instabilities).

In our configuration, a crude three-dimensional exploration has been performed and tends to confirm the two-dimensional character of the primary instability. Figure 17 displays the growth rate for a finite spanwise wavenumber $\beta^* = 0.5$, and for the wave vector angle of $\frac{\pi}{4}$ with respect to the streamwise direction (i.e. a spanwise wavenumber β^* equal to the streamwise wavenumber k^*). For these configurations, the growth rates are lower than in the 2D case. 2D instabilities grow more quickly: the flow remains two-dimensional in the primary instability phase.

Nevertheless, the flow eventually becomes three-dimensional at later time. A series of 3D numerical simulations have been carried out to evaluate the limits of the 2D approach.

The occurrence of streamwise vortices is observed at $t^* \sim 220$ through the creation of streamwise tubes of counter-rotating vorticity on vortex sheets. Figure 18 shows isovalues of the streamwise vorticity: each grey level represents the same amplitude for vorticity of opposite sign. Comparing with Figure 14(b), it seems that three-dimensionalisation inhibits vortex pairing. This is in agreement with recent observations in the ocean by Geyer et al (2010) who observed conservation of a kind of turbulent primary vortices under the action of secondary instabilities at large Reynolds number. This suggests that three-dimensional structures may play a role in the subsequent phase following the initial transient growth of the instability, and can therefore modify the final thickness of the mixing layer (see Peltier and Caulfield (2003)). Exploring such effects requires substantial computational resources. This topic is beyond the scope of the present paper and is left for future work.

5 Conclusion

We have set an idealized model of two layer mud-water flow, based on the incompressible Navier-Stokes equations with variable density and viscosity. This model aims at representing the hydrodynamic processes that destabilize the interface between mud flow and water at the bottom of estuaries. In the present study, mud flow is considered as a Newtonian fluid of high density and viscosity, miscible in water. At the interface, the mean velocity, density and viscosity profiles are represented by continuous asymmetric erf-shaped functions. We have performed a linear stability analysis by exploring a relevant range of control parameters k, Ri, Re and W and documented the influence of these parameters on the flow. We have complemented this linear approach with direct numerical simulations, and extended the study to
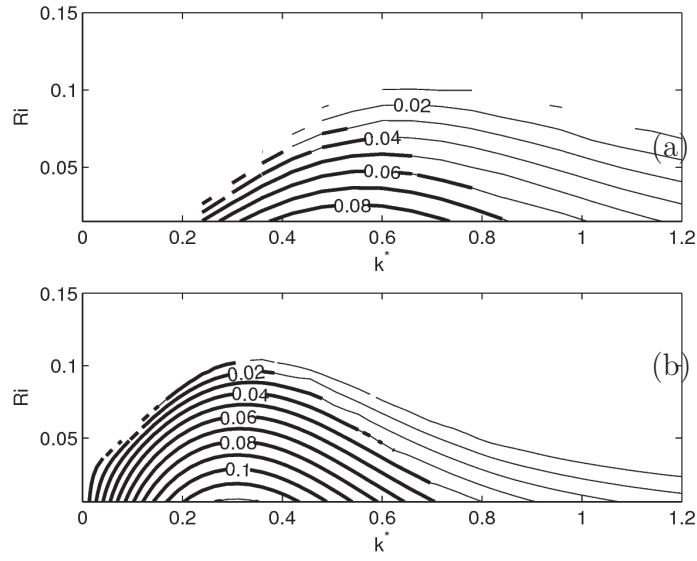
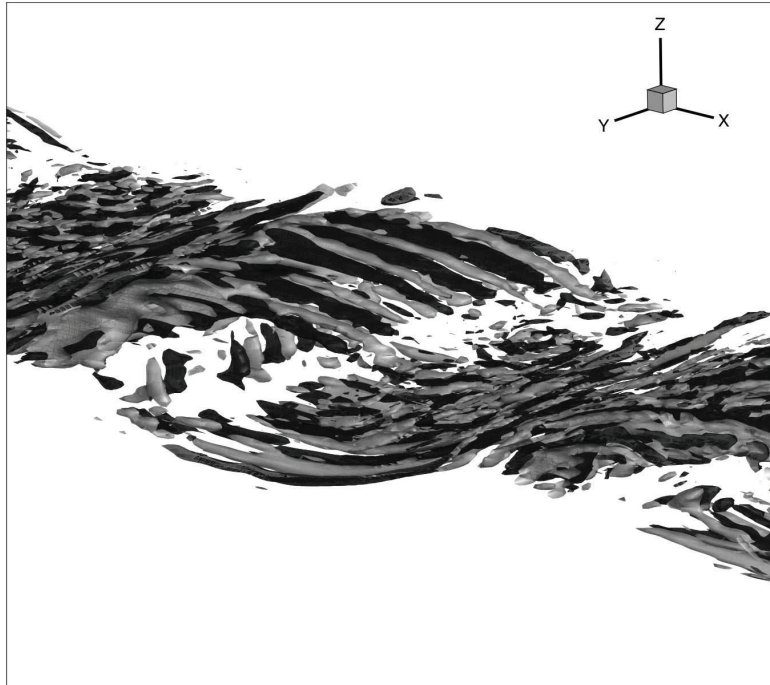Figure 17: Growth rate for 3D KH rolls, $W = 0$, $Re \sim 10^5$. (a): $\beta^* = 0.5$, (b): $\beta^* = k^*$

Figure 18: Isosurfaces of streamwise vorticity: three-dimensionalisation of the instability at $t^* = 220$ of $W = 2$, $Ri = 0.15$ and $Re = 10^3$.

28

the subsequent nonlinear development of the primary Kelvin-Helmholtz instability.

Results suggest that initial development of the instability is mainly controlled by the local Reynolds and Richardson numbers at the inflection point. The Richardson number at the inflection point, balancing stratification and shear effect, controls the development of the Kelvin-Helmholtz instability: Richardson numbers lower than the critical Richardson number ($Ri_c \sim 1/4$) lead to instability. For large Reynolds number, we show that there is no influence of the viscosity ratio nor of the Reynolds number on the linear development of the instability. For values lower than 10^3 approximately, the Reynolds number at the inflection point play a role: in particular, viscosity has a destabilizing influence. Increasing the viscosity ratio W promotes this destabilizing effect.

Direct numerical simulations reproduce these results in the short timed linear phase and complement the analysis: for small Reynolds numbers, the hypothesis of quasi-steady state of the mean flow is no longer justified. Evolution of the mixing layer with destabilization of the K-H rolls and pairing in the case of strong viscosity variation has also been presented. As commonly known, the final thickness of the interface is influenced by the Richardson number. The effect of viscosity stratification is also observed: for a given interfacial Reynolds number, viscosity stratification enhances the thickening of the interface by about 20%. Viscosity ratio influences the first destabilization of rolls and enhances the pairing occurrence in 2D configurations. Even though the pairing process seems to be inhibited for 3D configurations, it is likely that the viscosity stratification still enhances the growth of the mixing layer thickness.

Fully-resolved 3D simulations are needed to further document the evolution of the mixing layer and the influence of viscosity stratification. Mud viscosity impacts the linear and non-linear development of KH instability through viscous stratification and interfacial Reynolds number. Therefore mud viscosity has to be taken into account in entrainment parameterization. The types of estuarine systems of interest tend to evolve through temporal changing of the flow rate, that is they are subject to varying forcing Reynolds number. Therefore, the constant-Re flows considered in the present work are somewhat artificial. However, for such time evolving systems, the present linear stability analysis provides a way to evaluate stability of the interface and quantify the development of KH instabilities. The final thickness of the interface and vertical profiles will eventually be decisive to quantify bottom shear and turbulent flux of mass in realistic models.

The Reynolds number used in this study is computed at the cradle of the instability, i.e. at the interface, where viscosity is important. This explains the low values of this parameter explored by the present DNS simulations. However, this interfacial Reynolds number may be somewhat low for highly turbulent configurations or for low mud viscosity. In these cases, the results only give a first idea of the development of KH instabilities in a turbulent flow if one interprets the present viscosity values as those of a constant turbulent viscosity. In this view, the present results represent only a part of the interface evolution processes since turbulent mass diffusion, which can no longer be neglected, has to be taken into account. New simulations or experiments are needed to confirm the observed behavior of the interface

in fully turbulent configurations. To obtain even more precise and realistic results, the viscoplastic rheological behavior of the mud should also be taken into account, not only as a threshold for resuspension, but also in the evolution of the interface.

Acknowledgment

Appendix

In this appendix, we describe the method that we have developed to identify the discretised K-H modes among spurious modes tracing back the continuous spectrum of the linear problem.

Characterization of the spurious modes

Spurious modes are characterized by a Chebyshev decomposition of the z-profiles that is not converged. The associated spurious eigenvalues stand close to the marginal curve of null growth rate $\sigma^* = 0$. We interpret them as a continuous spectrum of internal waves trapped in critical layers. A physical hint of these modes can be caught by considering the refraction of plane internal waves by density stratification and shear. The WKB method describes the evolution of wave packets of the wave vector $k, m(z)$ in the two-dimensionnal plane (x, z). They form a solution of the Eikonale equation $\Omega[k, m(z), z] = \Omega_0$ with $\Omega(k, m, z) = \sqrt{\frac{g}{\rho_r} \frac{\partial \overline{\rho}}{\partial z}} \frac{k}{\sqrt{m^2+k^2}} + k \, \overline{u}(z)$ and Ω_0 constant, where ρ_r is the reference density used in the framework of a Bousinesq approximation of the Navier-Stokes equations.
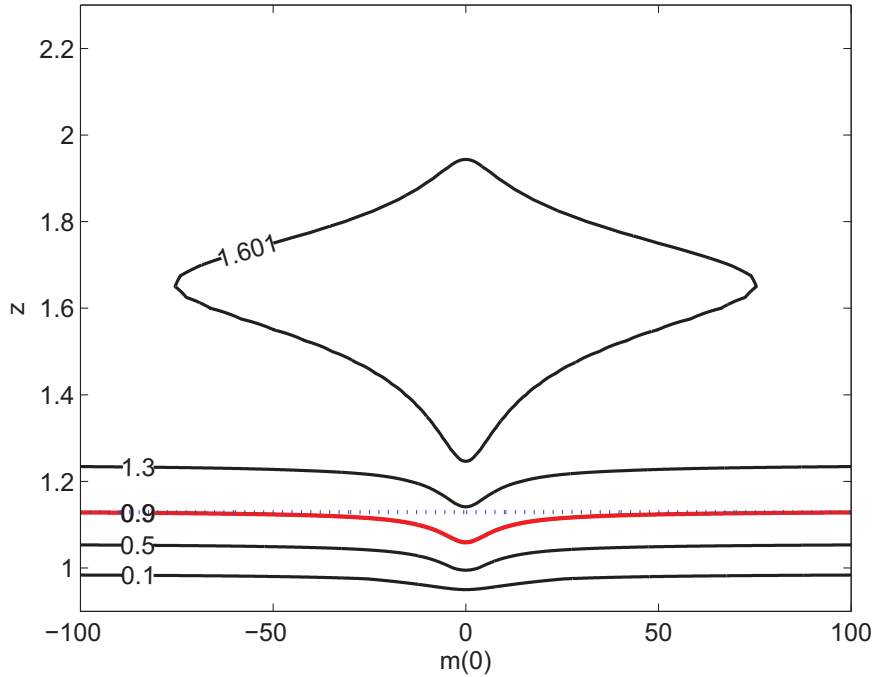

Figure 19: Isovalues of $\Omega[k, m(z), z]$ in the (m, z) plane for $Ri = 0, 15$, $k^* = 0, 8$, zoomed on $z \in [0.9, 2.3]$

Figure 19 presents isovalues of the frequency for fixed wave number, representing rays of internals waves, in the (m, z) plane. Divergent trajectories are observed and characterized by horizontals asymptotes (as dotted line for $\omega = 0.9$) with $m \to \infty$
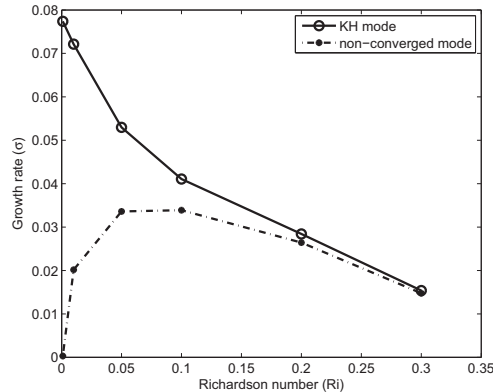
Figure 20: Growth rate of the two most unstable eigenmodes as a function of the Richardson number for $W = 0$, $k^* = 1.1$

and $z \to z_c$. These asymptotes correspond to absorption critical layers of internal waves. Due to viscosity, equation does not degenerate as Rayleigh equation for $\overline{u} = c$. Yet, very high resolution is needed since these layers present a thickness of $(k^* Re)^{-1/3}$ (see Drazin and Reid (1984)). Non-converged but physical modes with positive growth rate have their origin in these critical layers. To validate this hypothesis, the relation of dispersion $\omega \sim k\,\overline{u}(z_c)$ have been verified. Frequency of modes are compared to $k\,\overline{u}(z_c)$, by obtaining z_c from vertical profiles of the mode. Figure 21 shows that the growth rate of these modes decreases when resolution grows: they are under-resolved. Figure 20 shows that these modes also decrease around $Ri = 0$. This evolution corroborate the relation between modes and internal waves.
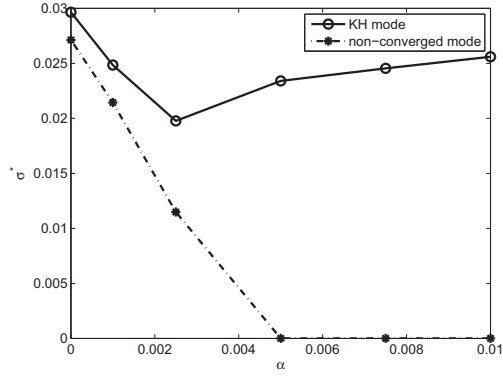
Complex mapping function

The elimination of these spurious modes at the profit of the searched K-H modes is achieved through the use of a complex mapping in the LiSa code. This stability code is based on a spectral decomposition using Chebyshev polynomials with a collocation method using a mapping transforming the spectral variable $s \in [-1, 1]$ (Gauss-Lobatto collocation points) into the physical variable z. A first real mapping $z = \varphi_0(s)$ reads:

$$\varphi_0(z) = C_1 \left[1 - e^{C_2 \operatorname{arctanh}(C_3 s) + C_4} \right] ,$$

where the constants C_1, C_2, C_3 and C_4 are adjusted to match the positions of the interface and the two boundaries as well as to adjust the refinement of the collocation grid near the interface. Based on an idea of Fabre et al (2006), we have extended it to the complex mapping $\varphi_\alpha(z) = \varphi_0(s)\,(1 - i\,\alpha)$ with $\alpha = 0.010369 - 0.035621\,Ri$. As presented on Figure 21(b), α can been determined through a sensitivity analysis of the eigenvalues with respect to its value. We choose the lowest value of α for which growth rate of spurious eigenvalues pass horizontal neutral axes (corresponding to their supposed position).

32
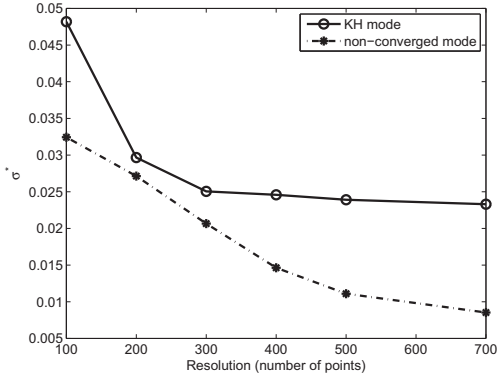
(a) Growth rate versus resolution   (b) Growth rate versus α

Figure 21: Growth rate of the two most unstable eigenmode, for $W = 3$, $k^* = 0.95$, $Re = 100$, $Ri = 0.15$. (a) Variation with the resolution. (b) Variation with α.

Figure 22 presents the eigenvalues spectrum for the two mappings. With the real mapping φ_0, the KH mode is "hidden" in a continuous spectrum of non-converged mode corresponding to internal waves trapped in absorption critical layers as presented earlier. With the complex mapping φ_α, the continuous spectrum is pushed below while the unstable KH-mode subsists and exhibit a converged Chebyshev decomposition. The use of the complex mapping is equivalent to a deformation of the integration path in the complex plane, which avoids the singularities at the z real points corresponding to the critical layers. The error done with a constant α mapping, which does not bring back the integration path towards the real axes, appears to be negligible for the eigenvalue precision looked at in the present work.
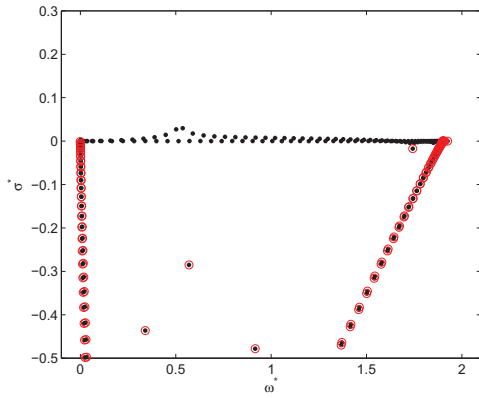
(a) Real mapping φ_0.
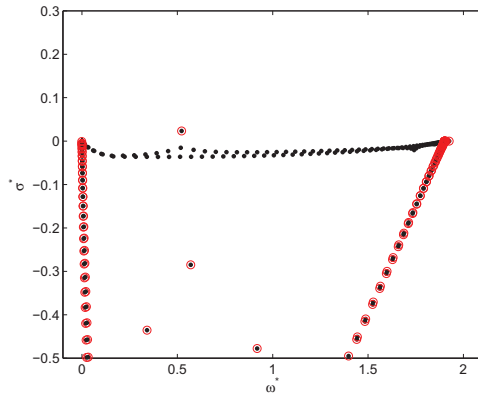
(b) Complex mapping φ_α.

Figure 22: Eigenvalues spectra for $Ri = 0.15$, $W = 3$, $Re = 10^2$, $k^* = 0.95$. Comparison of the real and compoex mappings. Eigenvalues with red circles correspond to converged modes.

References

Adams J C E, Wells JT, Park YA (1993) Nearshore and Estuarine Cohesive Sediment Transport, Coastal Estuarine Stud., vol 42, AGU, chap Wave motions on a lutocline above a stably stratified bottom boundary layer, pp 393–410. DOI 10.1029/CE042p0393, URL http://dx.doi.org/10.1029/CE042p0393

Amos CL, Umgiesser G, Ferrarin C, Thompson CEL, Whitehouse RJS, Sutherland TF, Bergamasco A (2010) The erosion rates of cohesive sediments in venice lagoon, italy. Continental Shelf Research 30(8):859 – 870, DOI 10.1016/j.csr.2009.12.001, URL http://www.sciencedirect.com/science/article/pii/S0278434309003471

Antkowiak A, Brancher P (2007) On vortex rings around vortices: an optimal mechanism. Journal of Fluid Mechanics 578:295–304, DOI 10.1017/S0022112007005198

Balmforth NJ, Roy A, Caulfield CP (2012) Dynamics of vorticity defects in stratified shear flow. Journal of Fluid Mechanics 694:292–331, DOI 10.1017/jfm.2011.548

Bonometti T, Balachandar S, Magnaudet J (2008) Wall effects in non-boussinesq density currents. Journal of Fluid Mechanics 616:445–475, DOI 10.1017/S002211200800414X, URL http://dx.doi.org/10.1017/S002211200800414X

Calmet I, Magnaudet J (1997) Large-eddy simulation of high-schmidt number mass transfer in a turbulent channel flow. Physics of Fluids 9(2):438–455, DOI 10.1063/1.869138

Carpenter JR, Balmforth NJ, Lawrence GA (2010) Identifying unstable modes in stratified shear layers. Physics of Fluids 22(5):054,104, DOI DOI:10.1063/1.3379845

Caulfield CP (1994) Multiple linear instability of layered stratified shear flow. Journal of Fluid Mechanics Digital Archive 258(-1):255–285, DOI 10.1017/S0022112094003320

Corcos GM, Lin SJ (1984) The mixing layer: deterministic models of a turbulent flow. part 2. the origin of the three-dimensional motion. Journal of Fluid Mechanics 139:67–95, DOI 10.1017/S0022112084000264

Corcos GM, Sherman FS (1984) The mixing layer: deterministic models of a turbulent flow. part 1. introduction and the two-dimensional flow. Journal of Fluid Mechanics 139:29–65, DOI 10.1017/S0022112084000252

Cugier P, Le Hir P (2002) Development of a 3d hydrodynamic model for coastal ecosystem modelling. application to the plume of the seine river (france). Estuarine Coastal And Shelf Science 55(5):673–695

Drazin PG, Reid WH (1984) Hydrodynamic Stability. Cambridge Mathematical Library, Cambridge Univ Press, DOI 10.2277/ 0521525411

Ern P, Charru F, Luchini P (2003) Stability analysis of a shear flow with strongly stratified viscosity. Journal of Fluid Mechanics 496:295–312, DOI 10.1017/S0022112003006372

Fabre D, Sipp D, Jacquin L (2006) Kelvin waves and the singular modes of the Lamb–Oseen vortex. Journal of Fluid Mechanics 551:235–274, DOI 10.1017/S0022112005008463

Fontane J, Joly L (2008) The stability of the variable-density kelvin-helmholtz billow. Journal of Fluid Mechanics 612:237–260, DOI 10.1017/S0022112008002966

Geyer WR, Lavery AC, Scully ME, Trowbridge JH (2010) Mixing by shear instability at high reynolds number. Geophys Res Lett 37, DOI 10.1029/2010GL045272

Govindarajan R (2004) Effect of miscibility on the linear instability of two-fluid channel flow. International Journal of Multiphase Flow 30(10):1177 – 1192, DOI 10.1016/j.ijmultiphaseflow.2004.06.006

Hallez Y, Magnaudet J (2009) A numerical investigation of horizontal viscous gravity currents. Journal of Fluid Mechanics 630:71–91, DOI 10.1017/S0022112009006454

Hardisty J (2007) Estuaries: Monitoring and Modeling the Physical System. Blackwell Publishing, DOI 10.1002/9780470750889.fmatter, URL http://dx.doi.org/10.1002/9780470750889.fmatter

Hazel P (1972) Numerical studies of the stability of inviscid stratified shear flows. Journal of Fluid Mechanics 51:39–61, DOI 10.1017/S0022112072001065

Healey JJ (2009) Destabilizing effects of confinement on homogeneous mixing layers. Journal of Fluid Mechanics 623:241–271, DOI 10.1017/S0022112008005284

Helmholtz Hv (1868) über discontinuirliche flüssigkeitsbewegungen. Monats Könibl Preuss Akad Wiss Berlin 23:215–228

Hinch EJ (1984) A note on the mechanism of the instability at the interface between two shearing fluids. Journal of Fluid Mechanics 144:463–465, DOI 10.1017/S0022112084001695

Holmboe J (1962) On the behaviour of symmetric waves in stratified shear layers. Geoflfs Publ 24:67–113

Hooper AP, Boyd WGC (1983) Shear-flow instability at the interface between two viscous fluids. Journal of Fluid Mechanics 128:507–528, DOI 10.1017/S0022112083000580

Jiang GS, Shu CW (1996) Efficient implementation of weighted ENO schemes. Journal of Computational Physics 126:202–228

Kelvin L (1871) Hydrokinetic solutions and observations. Phil Mag 42(4):362–377

Kranenburg C, Winterwerp JC (1997) Erosion of fluid mud layers. i: Entrainment model. Journal of Hydraulic Engineering 123(6):504–511, DOI 10.1061/(ASCE)0733-9429(1997)123:6(504)

Le Hir P, Cayocca F, Waeles B (2011) Dynamics of sand and mud mixtures: a multiprocess-based modelling strategy. Continental Shelf Research 10:S135–S149

Le Normant C (2000) Three-dimensional modelling of cohesive sediment transport in the Loire estuary. Hydrological Processes 14(13):2231–2243

Legendre D, Magnaudet J (1998) The lift force on a spherical bubble in a viscous linear shear flow. Journal of Fluid Mechanics 368:81–126, DOI null

Malik SV, Hooper AP (2005) Linear stability and energy growth of viscosity stratified flows. Physics of Fluids 17(2):024101, DOI 10.1063/1.1834931

Mashayek A, Peltier WR (2011) Three-dimensionalization of the stratified mixing layer at high reynolds number. Physics of Fluids 23(11):111701, DOI 10.1063/1.3651269

McAnally WH, Friedrichs C, Hamilton D, Hayter E, Shrestha P, Rodriguez H, Sheremet A, Teeter A, Task Committee on Management of Fluid Mud A (2007a) Management of fluid mud in estuaries, bays, and lakes. i: Present state of understanding on character and behavior. Journal of Hydraulic Engineering 133(1):9–22, DOI 10.1061/(ASCE)0733-9429(2007)133:1(9)

McAnally WH, Teeter A, Schoellhamer D, Friedrichs C, Hamilton D, Hayter, Shrestha P, Rodriguez H, Sheremet A, Kirby R, Task Committee on Management of Fluid Mud A (2007b) Management of fluid mud in estuaries, bays, and lakes. ii: Measurement, modeling, and management. Journal of Hydraulic Engineering 133(1):23–38, DOI 10.1061/(ASCE)0733-9429(2007)133:1(23)

Mehta AJ, Srinivas R (1993) Observations on the entrainment of fluid mud by shear flow. Coastal and Estuarine studies pp 224–224

Mehta AJ, H EJ, Parker WR, Krone RB, Teeter AM (1989) Cohesive sediment transport. i: Process description. Journal of Hydraulic Engineering 115:1076

Miles JW (1961) On the stability of heterogeneous shear flows. Journal of Fluid Mechanics 10(04):496–508, DOI 10.1017/S0022112061000305

Neumeier U, Ferrarin C, Amos CL, Umgiesser G, Li MZ (2008) Sedtrans05: An improved sediment-transport model for continental shelves and coastal waters with a new algorithm for cohesive sediments. Computers & Geosciences 34(10):1223 – 1242, DOI 10.1016/j.cageo.2008.02.007, URL http://www.sciencedirect.com/science/article/pii/S0098300408000538

Odd NV, Cooper AJ (1989) A two-dimensional model of the movement of fluid mud in a high energy turbid estuary. Journal of Coastal Research pp pp. 185–193

Orr WW (1907) The stability or instability of the steady motions of a perfect liquid and of a viscous liquid. Proceedings of the Royal Irish Academy Section A: Mathematical and Physical Sciences 27:9–68 and 69–138, URL http://www.jstor.org/stable/20490590

Ozdemir CE, Hsu TJ, Balachandar S (2011) A numerical investigation of lutocline dynamics and saturation of fine sediment in the oscillatory boundary layer. Journal of Geophysical Research: Oceans 116(C9), DOI 10.1029/2011JC007185, URL http://dx.doi.org/10.1029/2011JC007185

Ozgen S, Degrez G, Sarma GSR (1998) Two-fluid boundary layer stability. Physics of Fluids 10(11):2746–2757, DOI 10.1063/1.869798

Partheniades E (1965) Erosion and deposition of cohesive soils. J Hydraulics Division, ASCE 91(1):105–137

Patnaik PC, Sherman FS, Corcos GM (1976) A numerical simulation of kelvin-helmholtz waves of finite amplitude. Journal of Fluid Mechanics Digital Archive 73(02):215–240, DOI 10.1017/S0022112076001353

Peltier WR, Caulfield CP (2003) Mixing efficiency in stratified shear flows. Annual Review of Fluid Mechanics 35(1):135–167, DOI 10.1146/annurev.fluid.35.101101.161144

Rayleigh L (1879) On the stability, or instability, of certain fluid motions. Proceedings of the London Mathematical Society s1-11(1):57–72, DOI 10.1112/plms/s1-11.1.57

Sahu KC, Ding H, Valluri P, Matar OK (2009) Linear stability analysis and numerical simulation of miscible two-layer channel flow. Physics of Fluids 21(4):042104, DOI 10.1063/1.3116285

Sommerfeld A (1908) Ein beitrag zur hydrodynamischen erklaerung der turbulenten fluessigkeitsbewegungen. Proceedings 4th International Congress of Mathematicians, Rome 3:116–24

Squire HB (1933) On the stability for three-dimensional disturbances of viscous fluid flow between parallel walls. Proceedings of the Royal Society of London Series A, Containing Papers of a Mathematical and Physical Character 142(847):pp. 621–628

Srinivas R, Mehta A (1989) Observations on estuarine fluid mud entrainment. Int J Sed Res 5(1):15–22

Staquet C (1995) Two-dimensional secondary instabilities in a strongly stratified shear layer. Journal of Fluid Mechanics 296:73–126, DOI 10.1017/S0022112095002072

Staquet C (2000) Mixing in a stably stratified shear layer: two- and three-dimensional numerical experiments. Fluid Dynamics Research 27(6):367

Taylor G (1931) Effect of variation in density on the stability of superposed streams of fluid. Proceedings of the Royal Society of London Series A 132(820):499–523

Wolanski E, Asaeda T, Imberger J (1989) Mixing across a lutocline. Limnology and Oceanography 34(5):pp. 931–938

Yih CS (1955) Stability of two-dimensional parallel flows for three-dimensional disturbances. Quart Appl Math 4:434–425

Yih CS (1967) Instability due to viscosity stratification. Journal of Fluid Mechanics 27(02):337–352, DOI 10.1017/S0022112067000357